Author/s:
Mason, LR;Ciceri, D;Harvie, DJE;Perera, JM;Stevens, GW

Title:
Modelling of interfacial mass transfer in microfluidic solvent extraction: Part I. Heterogenous transport

Date:
2013-01-01

Citation:
Mason, L. R., Ciceri, D., Harvie, D. J. E., Perera, J. M. & Stevens, G. W. (2013). Modelling of interfacial mass transfer in microfluidic solvent extraction: Part I. Heterogenous transport. Microfluidics and Nanofluidics, 14 (1-2), pp.197-212. https://doi.org/10.1007/s10404-012-1038-z.

Persistent Link:
https://hdl.handle.net/11343/282896

Microfluid Nanofluid manuscript No.
(will be inserted by the editor)

Modelling of interfacial mass transfer in microfluidic solvent extraction

Part I. Heterogeneous transport

Lachlan R. Mason · Davide Ciceri · Dalton J. E. Harvie · Jilska M. Perera · Geoffrey W. Stevens

Received: date / Accepted: date

Abstract An investigation of molecular diffusion of solutes across water/oil interfaces in a Y-Y-shaped microchannel with an integrated guide structure is presented. Finite volume numerical simulations were compared with experimental literature data. Analytical approaches including an infinite composite medium model, phase-specific mass transfer coefficient models and a static transfer cell model were also assessed. An increase in accuracy for the mass transfer coefficient models was achieved by using local coefficients as opposed to length-averaged expressions. The static transfer cell model was shown to improve when based on the interfacial contact time, as opposed to the organic phase residence time. The results presented in this work have immediate application to the determination of kinetic rate constants in reactive mass transfer systems, as considered in Part II of this study (Ciceri D, Mason LR, Harvie DJE, Perera JM, Stevens GW (2012) Modelling of interfacial mass transfer in

L. R. Mason · D. Ciceri · D. J. E. Harvie · J. M. Perera · G. W. Stevens
Department of Chemical and Biomolecular Engineering
The University of Melbourne, Melbourne, VIC 3010, Australia
E-mail: gstevens@unimelb.edu.au

microfluidic solvent extraction. Part II. Heterogeneous transport with reaction. Microfluid Nanofluid Submitted).

Keywords Diffusion · Finite volume simulation · Liquid/liquid interface · Microfluidics · Solvent extraction

1 Introduction

Solvent extraction (SX), a widely exploited separations technique, makes use of a liquid/ liquid interface in driving solute separation. Unless under dilute reagent concentrations, reaction kinetics (if present) are generally fast and net extraction rates are controlled by molecular diffusion. Hence, the mechanistic and kinetic information associated with the reaction is not often experimentally resolvable using conventional approaches. This two-part study makes use of both modelling techniques and experimental data to demonstrate a method for the determination of this information using a microfluidic chip. As both diffusion and reaction are occurring, the diffusion-only case for this system was characterised (Part I) before introducing the added complexity of an interfacial reaction (Part II).

Interest in microfluidics and its application to lab-on-a-chip (LOC) systems is accelerating in the scientific community (Whitesides 2006). At the micro scale, inertial forces can commonly be neglected, allowing the dynamics of diffusive mass transfer (Crank 1975; Frank-Kamenetskii 1969) to be investigated using laminar flow (Kamholz and Yager 2001; Squires and Quake 2005). The need for numerical simulations and analytical frameworks to model microfluidic solvent extraction (μSX) experiments has renewed interest in diffusion theories for both homogeneous and heterogeneous systems. An overview of previous diffusion studies using microfluidic devices is shown in Table 1.

Homogeneous systems are those in which two miscible fluids with different solute concentrations are brought together. These include the Laminar Fluid Diffusion Interface experiments of van Leeuwen et al. (2009), in which the concentration of the solute diffusing between the streams is monitored as a function of the system residence time. Variable parameters include the choice of solute and the cross-sectional profile of the microchannel. Under laminar flow conditions, solute diffusion can be modelled accurately using Fick's laws (Fick 1855). Methods of modelling homogeneous systems increase in complexity from engineering-type correlations and analytical expressions to full three-dimensional computational fluid dynamics (CFD) simulations. Hotta et al. (2007) proposed a mass transfer coefficient model to determine the diffusion coefficients of benzoic acid, sucrose and glycine in water from experimental results. Kamholz et al. (1999) used a one-dimensional advection-diffusion equation to investigate diffusion in a T-shaped planar channel. The two streams were assumed to have equal viscosities and only the average fluid velocity was included in the governing transport equations. Kamholz and Yager (2001) investigated the effect of a non-uniform velocity profile on the solute concentration using a two-dimensional advection-diffusion equation. Full three-dimensional simulations, in which the advection-diffusion and Navier-Stokes equations are coupled, have recently been undertaken (Broboana et al. 2011; van Leeuwen et al. 2009; Nishi et al. 2010). Van Leeuwen et al. (2009) compared simulation results to an experimental study of the diffusion of glucose in water using an H-shaped microchannel of trapezoidal cross-section. Numerical and experimental results were in agreement indicating that a CFD approach is a reliable method for modelling microfluidic systems. Nishi et al. (2010) simulated the homogeneous diffusion of Co^{II} ions in an aqueous phase and a Co-DEHPA complex in decane; a trial-and-error optimisation method allowed calculation of the solute diffusion coefficients using a fully-developed flow assumption. Broboana et al. (2011) studied the transient diffusion of a tetramethyl rhodamine (TRM)

fluorescent tracer in an aqueous solvent using a Y-shaped planar channel. The asymmetric distribution of the solute concentration ('butterfly effect'), due to slower solvent velocities in close proximity to the walls, was discussed in detail.

Heterogeneous systems, first examined in a μSX context by Sato et al. (2000), differ from homogeneous systems in that the two streams brought together are immiscible. These systems have not been investigated as extensively as homogeneous systems (Ciceri et al. 2011a) primarily due to the difficulty of achieving a stable flow between immiscible fluids in the micro environment (Aota et al. 2009; Smirnova et al. 2006; Tetala et al. 2009). Surmeian et al. (2002) used a two-layer microchannel to determine the partition coefficient of methyl red over a water/cyclohexane interface. A one-dimensional diffusion-driven model was developed neglecting effects of the fluid flow. Ciceri et al. (2011a) modified the one-dimensional static transfer cell equation of McCulloch et al. (1996) to model solute diffusion in a heterogeneous system. Incorporation of the organic-phase residence time and a cross-sectional-area-equivalent height was proposed in order to extend the model to different geometries encountered in microfluidic experiments. Good agreement was shown for both homogeneous and heterogeneous diffusion systems in the absence of chemical reactions. Two-dimensional (Tetala et al. 2009) and three-dimensional (Žnidaršič-Plazl and Plazl 2007) CFD simulations of solute diffusion in two-phase systems have been presented. Tetala et al. (2009) investigated the extraction, followed by immediate back extraction, of strychnine for a water/chloroform system in a Y-Y-shaped microchannel with semi-toroidal pillar structures. Žnidaršič-Plazl and Plazl (2007) simulated the extraction of progesterone, incorporating interfacial solute transfer over a water/ethyl acetate interface in a serpentine channel. Kuban et al. (2003) studied vertically stratified flows in water/butanol and water/chloroform systems using a planar channel, with application to the extraction of methylene blue in water/alcohol systems. A volume-of-fluid numerical method, allowing inclusion of surface tension forces

Table 1: Overview of experimental conditions for microfluidic diffusion experiments

Source	Solute	Contacting phases	$\mathscr{D}_{aq}$ (m^2/s)	$\mathscr{D}_{org}$ (m^2/s)
Hotta et al. (2007)	benzoic acid	aq/aq	9.0×10^{-10}	N/A
Ibid.	sucrose	aq/aq	5.2×10^{-10}	N/A
Ibid.	glycine	aq/aq	1.2×10^{-9}	N/A
van Leeuwen et al. (2009)	glucose	aq/aq	6.7×10^{-10}	N/A
Nishi et al. (2010)	Co^{II}	aq/aq	6.6×10^{-10}	N/A
Ibid.	Co-DEHPA	decane/decane	N/A	3.2×10^{-10}
Ciceri et al. (2011a)	8-hydroxyquinoline	aq/heptane	1.4×10^{-9}	2.2×10^{-9}
Surmeian et al. (2002)	methyl red	aq/cyclohexane	5.4×10^{-10}	7.2×10^{-10}
Žnidaršič-Plazl and Plazl (2007)	progesterone	aq/ethyl acetate	4.3×10^{-10}	1.3×10^{-9}
Ibid.	11α-hydroxyprogesterone	aq/ethyl acetate	4.0×10^{-10}	1.3×10^{-10}

normal to the interfacial plane, was used to predict the observed flow regime, however solute diffusion was not modelled. Pohar et al. (2012) used a finite difference method to determine the interface location in heterogeneous systems. Effects of interfacial tension were assumed negligible and a planar interface modelled. Non-reactive systems, in which the solubility of the organic phase in water is negligible, were used in only the minority of these studies (Ciceri et al. 2011a; Surmeian et al. 2002).

In the present study, independent sets of experimental data, specific to heterogeneous systems, were analysed from the literature. The selected microchannel system is Y-Y shaped with an integrated guide structure used to stabilise the interface. A comparison was made with results from finite volume numerical simulations, and the suitability of using simplified analytical models based on phase-specific mass transfer coefficients was also investigated. Results have direct application to the interpretation of diffusion data in heterogeneous liquid/ liquid systems.

2 Numerical simulation

CFD techniques were used to simulate both diffusion throughout the liquid volumes and partitioning of species across the interface. A finite volume algorithm, *arb* (Harvie 2012), was

used to simulate data from appropriate microfluidic studies (Ciceri et al. 2011a; Surmeian et al. 2002). Two notable assumptions were used to simplify the computations: (i) the interface was assumed to be flat and (ii) the velocity profile in both streams was assumed to be fully developed.

2.1 Treatment of the interface

The use of an integrated guide structure has been previously adopted to stabilise the laminar flow in heterogeneous diffusion experiments (Aota et al. 2009; Ciceri et al. 2011a; Tokeshi et al. 2000). In the simulations, a flat interface was assumed for the entire pass length. Interfacial tension, therefore, was not used to balance the normal shear stress across the interface. The volumetric flow rates for each phase, governed by independent x-direction pressure gradients, were then set to the corresponding experimental values. To assess the accuracy of this assumption, the magnitude of interfacial curvature in the real system was estimated. The maximum curvature of the interface will occur at the beginning of the pass length and can be approximated by equating the pressure difference between the two streams, due to frictional losses, and the Laplace pressure due to interfacial tension (Aota et al. 2007). As shown in Online Resource 1, the maximum interfacial contact angle $\theta_{\max}$ can be expressed as

$$\theta_{\max} = \frac{\pi}{2} + \arcsin\left[\frac{16Ld}{\gamma D_{\mathrm{h}}^2}\left(\mu_{\mathrm{aq}}\bar{u}_{x,\mathrm{aq}} - \mu_{\mathrm{org}}\bar{u}_{x,\mathrm{org}}\right)\right], \tag{1}$$

where $\bar{u}_{x,\mathrm{aq}}$ and $\bar{u}_{x,\mathrm{org}}$ are the mean fluid velocities, L is the pass length, d is the z-height of the interface, D_{h} is the hydraulic diameter and γ is the interfacial tension. A measure of the maximum interfacial deformation in the y-direction, $\tilde{y}$, is given by:

$$\tilde{y} = R\left[1 - \cos\left(\frac{\phi}{2}\right)\right], \tag{2}$$

where $\phi = 2\theta_{\max} - \pi$ is the maximum angle subtended by the interfacial arc and $R = d/[2\sin(\phi/2)]$ is the radius of curvature. As shown in Online Resource 1, the maximum deformation for the data of Surmeian et al. (2002) was determined to be less than 1% of D_{h}, corresponding to an increase in the total interfacial area of 0.02%. For the experimental data of Ciceri et al. (2011a), the absence of significant interfacial curvature was observed visually.

In the original experiments, the flow rate ratio $F_{\mathrm{org}}/F_{\mathrm{aq}}$ was set such that the interface was located at the centreline of the microchannel. For the simulations, the interface was fixed at the centreline and the corresponding experimental flow rate values were used as inputs for each data point.

2.2 Momentum balance equations

The fluid velocity $\mathbf{u}$ was determined by solving the steady-state Navier-Stokes and incompressible continuity equations in conservative form:

$$\nabla \cdot (\rho_i \mathbf{u}\mathbf{u} + p_i \boldsymbol{I} + \boldsymbol{\tau}_i) = \mathbf{0} \tag{3}$$

$$\nabla \cdot \mathbf{u} = 0 \tag{4}$$

where ρ_i is the density of fluid i, p_i is the dynamic pressure and $\boldsymbol{\tau}_i$ is the viscous stress tensor. Gravitational effects were assumed negligible ($Bo = \Delta\rho g D_{\mathrm{h}}^2/\gamma \ll 1$ for all cases considered).

Velocity disturbances due to flow development were assumed to be negligible. Simulations performed using a complete Y-Y mesh (see Figure 1a for details of the geometry) indicated that the development length was less than $\sim 1\%$ of the pass length L, commensurate with previous studies (Žnidaršič-Plazl and Plazl 2007; Pohar et al. 2012). For all simulation results presented, only the pass length segment of the microchannel was used, corresponding to the 'simplified mesh' method (Nishi et al. 2010, 2011). Hence, the fluid velocity was

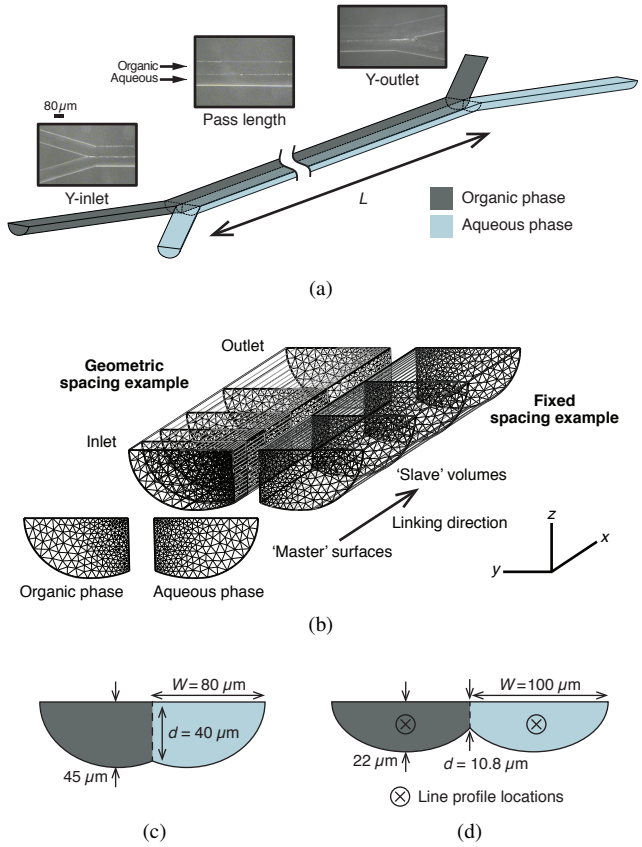

Fig. 1: (a) Two-phase microchannel schematic, (b) illustration of 'simplified mesh' geometry of pass length showing use of 'master' and 'slave' regions, adaptive mesh resolution, fixed and geometric x-direction spacing, (c) Ciceri et al. (2011a,b) cross-sectional geometry, (d) Surmeian et al. (2002) cross-sectional geometry and locations of line profiles (into the page)

assumed to be fully developed in the x-direction:

$$\frac{\partial u_x}{\partial x} = 0; \quad u_y = 0; \quad u_z = 0\,. \tag{5}$$

Applying the continuity equation and fully-developed flow assumption (Eqs. 4 and 5 respectively) allows the Navier-Stokes equation (Eq. 3) to be reduced to

$$\frac{\partial p}{\partial x} = \mu \left(\frac{\partial^2 u_x}{\partial y^2} + \frac{\partial^2 u_x}{\partial z^2} \right). \tag{6}$$

The fluid velocity was assumed to be continuous over the two-phase interface:

$$u_x\big|_{y \to y_{\text{int}}^-} = u_x\big|_{y \to y_{\text{int}}^+}, \tag{7}$$

where y_{int} is the y-coordinate of the interface. The interface of the heterogeneous system was assumed to be mobile, consistent with literature imaging studies (Akpa et al. 2007) and previous models (Pohar et al. 2012). The flux of x-momentum was set to be equal on both sides of the interface:

$$\mu_{\text{aq}} \left. \frac{\partial u_x}{\partial y} \right|_{y \to y_{\text{int}}^-} = \mu_{\text{org}} \left. \frac{\partial u_x}{\partial y} \right|_{y \to y_{\text{int}}^+} \tag{8}$$

$$\mu_{\text{aq}} \left. \frac{\partial u_x}{\partial z} \right|_{y \to y_{\text{int}}^-} = \mu_{\text{org}} \left. \frac{\partial u_x}{\partial z} \right|_{y \to y_{\text{int}}^+} \tag{9}$$

A no-slip velocity boundary condition was assumed on all walls.

2.3 Species balance equations

The local solute concentration c_i was determined using the steady-state advection-diffusion equation

$$\nabla \cdot (c_i \mathbf{u} - \mathscr{D}_i \nabla c_i) = 0, \tag{10}$$

where $\mathscr{D}_i$ is the diffusivity of the solute in phase i. An infinitely-thin two-phase interface was assumed, implying a jump discontinuity in the local solute concentration:

$$c_{\text{org,int}} = K_{\text{D}} c_{\text{aq,int}}\,, \tag{11}$$

where K_{D} is the distribution coefficient. Conservation of mass was implemented using a flux matching condition:

$$\mathscr{D}_{\text{org}} \left.\frac{\partial c}{\partial y}\right|_{y\to y_{\text{int}}^{+}} = \mathscr{D}_{\text{aq}} \left.\frac{\partial c}{\partial y}\right|_{y\to y_{\text{int}}^{-}}\,. \tag{12}$$

A no-flux condition was assumed on all walls:

$$\hat{\mathbf{n}} \cdot \nabla c = 0\,, \tag{13}$$

where $\hat{\mathbf{n}}$ is a unit normal vector local to each wall. The solute concentration was assumed to be constant over the inlet cross-sectional area:

$$c|_{x\in\text{inlet}} = c_0\,. \tag{14}$$

The outlet concentration was assumed to be fully developed in the direction of flow:

$$\left.\frac{\partial c}{\partial x}\right|_{x\in\text{outlet}} = 0\,. \tag{15}$$

2.4 Numerical implementation

The flow domain was split along the centreline into two separate mesh volumes with a flat interface as shown in Figure 1b, allowing accurate treatment of jump discontinuities in the solute concentration and solvent physical properties. Use of a split-domain method reduced the simulation error associated with the averaging of physical properties across

Table 2: Mesh resolutions used for three-dimensional computations

	Mesh 1A	Mesh 1B	Mesh 2	Mesh 3
Prisms	8,610	49,024	69,600	205,320
x-direction spacing	Fixed	Geometric	Fixed	Fixed

the interface (Online Resource 1). The simplified Navier-Stokes equation, Eq. 6, was then solved on two-dimensional 'master' surfaces and the solution extruded, or 'linked', to the corresponding three-dimensional 'slave' volumes. The advection-diffusion equation, Eq. 10, was then solved on the three-dimensional 'slave' domain.

Simulation mesh files were generated using the open-source application *Gmsh* (Geuzaine and Remacle 2009). A Delaunay triangulation algorithm (George and Borouchaki 1998) was used for the generation of two-dimensional unstructured master surfaces. The master surfaces were then extruded in the third dimension to form triangular prisms. To ensure accuracy of the simulations, the mesh resolution was increased close to the interface and microchannel inlet, where the maximum concentration gradients were observed to occur. The x-direction grid spacing used either a fixed or geometric progression, as illustrated in Figure 1b. Properties of the various meshes used for resolution independence testing purposes are shown in Table 2. The difference between results obtained using the most coarse and fine mesh was found to be less than 2%.

3 Analytical modelling

3.1 Infinite composite medium

Crank (1975) considered solutions to the one-dimensional diffusion equation (Fick's second law):

$$\frac{\partial c_i}{\partial t} = \mathscr{D}_i \frac{\partial^2 c}{\partial y^2} \,. \tag{16}$$

Analytical expressions for an infinite composite medium were derived using interfacial boundary conditions identical to Eqs. 11 and 12. Additionally, the solute concentration was assumed to remain constant for $y \to \pm\infty$, which is accurate for short diffusion time scales ($t \ll D_\mathrm{h}^2/\mathscr{D}_i$). If the interface is taken to be located at the origin, $y_\mathrm{int} = 0$, then:

$$c_\mathrm{aq}(t,y) = \Xi \left[1 + K_\mathrm{D} \sqrt{\frac{\mathscr{D}_\mathrm{org}}{\mathscr{D}_\mathrm{aq}}} \operatorname{erf} \frac{y}{2(\mathscr{D}_\mathrm{aq} t)^{1/2}} \right] , \quad y > 0 \tag{17}$$

$$c_\mathrm{org}(t,y) = K_\mathrm{D} \Xi \operatorname{erfc} \frac{|y|}{2(\mathscr{D}_\mathrm{org} t)^{1/2}} , \quad y < 0 \tag{18}$$

where $\Xi = c_\mathrm{aq,inlet} \left(1 + K_\mathrm{D} \sqrt{\mathscr{D}_\mathrm{org}/\mathscr{D}_\mathrm{aq}} \right)^{-1}$, erf and erfc refer to the error function and complementary error function respectively. In order to adapt Eqs. 17 and 18 for application to the present system (denoted 'infinite composite medium'), width averaging over the hydraulic diameter D_h was used to represent the bulk concentrations:

$$\tilde{c}_\mathrm{aq}(t) = \frac{1}{D_\mathrm{h}} \int_0^{D_\mathrm{h}} c_\mathrm{aq}(t,y) \,\mathrm{d}y \tag{19}$$

$$\tilde{c}_\mathrm{org}(t) = \frac{1}{D_\mathrm{h}} \int_{-D_\mathrm{h}}^{0} c_\mathrm{org}(t,y) \,\mathrm{d}y \tag{20}$$

Use of the hydraulic diameter enables application of the one-dimensional model to the present microchannel geometry.

The outlet concentration was then determined by setting t equal to the characteristic contact time scale t^*. Here, t^* was estimated using the organic phase residence time t_{org} (contact time scales are further discussed in Section 3.3).

3.2 Mass transfer coefficient models

Analogous to the heat transfer flux in a simple parallel-flow heat exchanger, the average diffusive flux $\tilde{J}_y$ of solute in the y-direction of the Y-Y microchannel system can be expressed (Truskey et al. 2004) in terms of an effective mass transfer coefficient K_{eff} as

$$\begin{aligned}\tilde{J}_y &= K_{\mathrm{eff}} \frac{\Delta\bar{c}_{\mathrm{outlet}} - \Delta\bar{c}_{\mathrm{inlet}}}{\ln\left(\dfrac{\Delta\bar{c}_{\mathrm{outlet}}}{\Delta\bar{c}_{\mathrm{inlet}}}\right)} \\ &= K_{\mathrm{eff}}\,(\Delta\bar{c})_{\mathrm{LM}}\,, \end{aligned} \tag{21}$$

where:

$$\Delta\bar{c}(x) \stackrel{\mathrm{def}}{=} \bar{c}_{\mathrm{aq}}(x) - \frac{\bar{c}_{\mathrm{org}}(x)}{K_{\mathrm{D}}} \tag{22}$$

$$K_{\mathrm{eff}} \stackrel{\mathrm{def}}{=} \left(\frac{1}{k_{\mathrm{aq}}} + \frac{1}{k_{\mathrm{org}} K_{\mathrm{D}}}\right)^{-1} \tag{23}$$

Here, overbars denote the velocity-averaged concentration over the cross-sectional area of each stream, lying in the yz plane,

$$\bar{c}_i(x) = \frac{\int c_i(x,y,z) u_x(y,z)\,\mathrm{d}A}{\int u_x(y,z)\,\mathrm{d}A}\,, \tag{24}$$

and k_{aq}, k_{org} are the average mass transfer coefficients. Four separate treatments were used for estimating the values of k_i.

3.2.1 Transfer coefficient model A

The average and local mass transfer coefficients were estimated, here, using penetration theory (Crank 1975; Higbie 1935). In the first case (denoted 'averaged coefficient A'), k_i were estimated using the average mass transfer coefficient derived from penetration theory for a semi-infinite medium (Hotta et al. 2007). For short time scales (taken to be $t^* \ll D_{\mathrm{h}}^2/\mathscr{D}_i$) the average transfer coefficient is given by:

$$\tilde{k}_i = 2\sqrt{\frac{\mathscr{D}_i}{\pi t^*}}\,. \tag{25}$$

The organic phase residence time ($t^* = t_{\mathrm{org}}$) has been used as an approximation for the characteristic contact time scale (contact time scales are further discussed in Section 3.3).

In the second case ('local coefficient A'), the local mass transfer coefficient for a semi-infinite medium (Crank 1975) was used:

$$k_i(t) = \sqrt{\frac{\mathscr{D}_i}{\pi t}}\,, \tag{26}$$

where t is the elapsed time of contact between the phases since entering the microchannel. The approximation

$$\frac{t}{t^*} \approx \frac{x}{L} \tag{27}$$

was used in order to express the local mass transfer coefficient in terms of the x-distance travelled:

$$k_i(x) = \sqrt{\frac{\mathscr{D}_i L}{\pi t^*}}\,x^{-1/2}\,. \tag{28}$$

A differential form of Eq. 21 was then integrated over the length of the microchannel (Eq. A.25 in Appendix A), which enabled the x-dependence of k_i to be explicitly incorporated into the model.

For both cases, the outlet solute concentration $\bar{c}_{\mathrm{org,outlet}}$ was determined by simultaneously solving Eq. 21 and the component mass balance equation

$$\sum_i F_i \bar{c}_{i,\mathrm{inlet}} = \sum_i F_i \bar{c}_{i,\mathrm{outlet}}\,, \tag{29}$$

where F_i is the volumetric flow rate of phase i.

3.2.2 Transfer coefficient model B

The average and local mass transfer coefficients were estimated, here, using the correlations of van Male et al. (2004). In the first case ('averaged coefficient B'), $\tilde{k}_i$ were expressed in terms of the phase-specific average Sherwood numbers $\tilde{Sh}_i$ as

$$\tilde{k}_i = \frac{\mathscr{D}_i}{D_\mathrm{h}} \tilde{Sh}_i\,. \tag{30}$$

The values of $\tilde{Sh}_i$ were estimated using the correlation (van Male et al. 2004):

$$Sh_i(x) = 2.43 \left(1 + \left[\frac{Gz_i(x)}{132} \right]^{0.835} \right), \tag{31}$$

where $Gz_i(x) = Re_i Sc_i D_\mathrm{h}/x$ is the Graetz number for mass transport, $Re = \rho_i \bar{u}_i D_\mathrm{h}/\mu_i$ is the Reynolds number and $Sc = \mu_i/\rho_i \mathscr{D}_i$ is the Schmidt number. Eq. 31 was averaged using

$$\tilde{Sh}_i = \frac{1}{L} \int_0^L Sh_i(x)\,\mathrm{d}x\,. \tag{32}$$

Note that Eq. 31 is valid for laminar flow in a square microchannel with mass transport occurring through one wall (and a no-flux condition on all others), so is only an approximation for our system. Laminar flow conditions have been confirmed for the present system (phase-specific Reynolds numbers are tabulated in Online Resource 1). For flow rate ratios close to unity, the velocity profile will be flat in close proximity to the interface. Hence, the plug flow correlation of van Male et al. (2004) was also trialled:

$$Sh_i(x) = 2.467\left(1+\frac{Gz_i(x)}{27.3}\right)^{0.407}. \tag{33}$$

In the second case ('local coefficient B'), the local mass transfer coefficient was used:

$$k_i(x) = \frac{\mathscr{D}_i}{D_\mathrm{h}} Sh_i(x)\,. \tag{34}$$

As per Section 3.2.1, a differential form of Eq. 21 was then integrated over the length of the channel. For both cases, $\bar{c}_{\mathrm{org,outlet}}$ was determined as per Section 3.2.1.

3.3 Static transfer cell model (STCM)

McCulloch et al. (1996) solved a one-dimensional diffusion equation for a static transfer cell. Ciceri et al. (2011a) adapted this equation for use in a dynamic microfluidic system by considering the characteristic time scale t^* of the device

$$\tilde{c}_{\mathrm{org,outlet}} = \frac{K_\mathrm{D}\tilde{c}_{\mathrm{aq,inlet}}}{(1/\mathscr{D}_\mathrm{org}^{1/2})+(K_\mathrm{D}/\mathscr{D}_\mathrm{aq}^{1/2})}\frac{2(t^*)^{1/2}}{h_\mathrm{norm}\pi^{1/2}}\,, \tag{35}$$

where $h_\mathrm{norm} = h_\mathrm{eq}F_\mathrm{org}/F_\mathrm{aq}$ and h_eq is a cross-sectional-area-equivalent height. Eq. 35 is valid in the small-time limit ($t^* \ll h_\mathrm{norm}^2/\mathscr{D}_i$).

Due to the development of a complex three-dimensional velocity profile, determination of the appropriate characteristic time scale is nontrivial. The average residence time of one phase can been used (Ciceri et al. 2011a,b; Hotokezaka et al. 2005). For example, defining the residence time based on the organic phase gives

$$t_{\mathrm{org}} = \frac{V_{1/2}}{F_{\mathrm{org}}}, \tag{36}$$

where $V_{1/2}$ is the microchannel half-volume. Alternatively, the average interfacial contact time t_{int} can be used (Hotta et al. 2007), requiring determination of the interfacial velocity by numerical simulation. The mean interfacial velocity can be determined based on the solution to Eq. 6 using

$$\bar{u}_{\mathrm{int}} = \frac{\int u_x|_{y_{\mathrm{int}}}\,\mathrm{d}z}{\int \mathrm{d}z}, \tag{37}$$

where the integral is taken over the z-direction line defining the organic interface of the 'master' mesh file in Figure 1b. The interfacial contact time t_{int} can then be determined using

$$t_{\mathrm{int}} = \frac{L}{\bar{u}_{\mathrm{int}}}. \tag{38}$$

An alternative method of estimating t_{int} was developed by modifying a two-dimensional analytical result for two-phase flow in a thin slit (Bird et al. 2002). The expression of Bird et al. (2002) was modified to include two phase-specific pressure gradients as detailed in Appendix B. The pressure gradients were set such that the experimental flow rates were matched. The interfacial contact time t_{int} can then be determined using the centreline interfacial velocity:

$$t_{\mathrm{int}} = \frac{L}{u_{\mathrm{int}}} = 2\left(\frac{L}{D_{\mathrm{h}}}\right)^2\left(\frac{\mu_1+\mu_2}{\Delta p_1+\Delta p_2}\right). \tag{39}$$

A Hele-Shaw model (Nadim et al. 1996), adapted for the present geometry, was also considered, however this model was not as accurate in predicting the interfacial contact time as Eq. 39. The present study aims to assess the validity of using either t_{org} or t_{int} for the characteristic time scale t^* in Eq. 35. Use of t_{org} is denoted 'STCM' (Static Transfer Cell Model). The values of t_{int} were estimated using two different methods: use of the thin slit expression (Bird et al. 2002) is denoted 'modified STCM A' and use of the full finite volume simulation is denoted 'modified STCM B'.

4 Details of original experiments

4.1 8-hydroxyquinoline solute

The diffusion of 8-hydroxyquinoline (8HQ) solute across an aqueous/heptane interface was modelled based on the experimental work of Ciceri et al. (2011a). Properties used are shown in Table 3. Outlet velocity-averaged solute concentrations $\bar{c}_i$ were generated for all models. As vial sampling was used, this form represents the concentration measured in the original experiment.

Table 3: Physical properties used for simulation of Ciceri et al. (2011a) experimental data. Reference conditions are 1 atm and 293 K

	Aqueous phase	Organic phase
c_0 (mM)	0.266	0
$\mathscr{D}_i$ (m^2/s)	1.4×10^{-9} [a]	2.2×10^{-9} [a]
μ_i (Pa s)	1.0×10^{-3} [b]	4.3×10^{-4} [c]
ρ_i (kg/m^3)	998[d]	686[c]
K_{D} (-)	44.8[a]	
L (m)	0.02	
D_{h} (μm)	54	

[a] McCulloch et al. (1996)
[b] Lide (2009)
[c] Yaws (2003)
[d] Perry and Green (2007)

Table 4: Properties used for simulation of Surmeian et al. (2002) experimental data. Reference conditions are 1 atm and 293 K

	Aqueous phase	Organic phase
c_0 (mM)	7.4×10^{-3}	0
F_i (mL/hr)	3.0×10^{-2}	3.0×10^{-2}
$\mathscr{D}_i$ (m^2/s)	5.4×10^{-10}	7.2×10^{-10}
μ_i (Pa s)	1.0×10^{-3} [a]	9.6×10^{-4} [b]
ρ_i (g/cm^3)	998[c]	780[b]
K_D (-)	0.91	
L (m)	0.03	
D_h (μm)	30	

[a] Lide (2009)
[b] Yaws (2003)
[c] Perry and Green (2007)

4.2 Methyl red solute

The diffusion of a methyl red solute across an aqueous/cyclohexane interface was modelled based on the experimental work of Surmeian et al. (2002). Properties used are shown in Table 4. A line profile along each half-volume centreline was generated as shown in Figure 1d. The average solute concentration for a given x-coordinate was also determined using

$$\tilde{c}_i(x) = \frac{\int c_i(x,y,z)\,\mathrm{d}A}{\int \mathrm{d}A}\,, \tag{40}$$

where the integral is taken over the cross-sectional yz plane (for each phase) located at the given x-coordinate. Note that this is not the same as the velocity-averaged concentration defined previously in Eq. 24 as a comparison is now being made to thermal lens microscopy (TLM) (Harada et al. 1993; Minagawa et al. 2001) line profile data.

5 Results and discussion

A summary of all model results for the 8HQ experimental data (Ciceri et al. 2011a) is shown in Table 5. Corresponding model results for the methyl red experimental data (Surmeian et al.

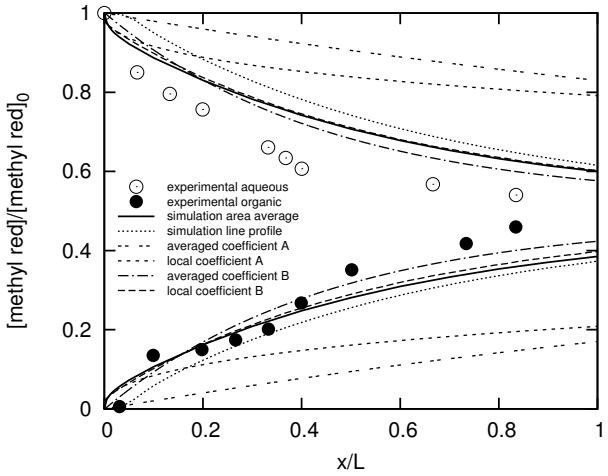

Fig. 2: Model results for the two-layer-flow methyl red experimental data of Surmeian et al. (2002). Finite volume simulation uses the highest resolution mesh (Mesh 3 in Table 2). Experimental data reprinted with permission from Surmeian et al. (2002). Copyright 2002 American Chemical Society

2002) are shown in Figure 2. In order to assess the relative errors associated with each model, the Mean Absolute Percentage Error (MAPE) was determined for each data set. Two separate MAPE values were calculated, with either the experimental concentration (MAPE_{exp}) or the simulation concentration (MAPE_{sim}) acting as the reference value in the denominator:

$$\text{MAPE}_{\text{exp}} = \frac{1}{N}\sum_{n=1}^{N}\left|\frac{\bar{c}_{\text{exp},n} - \bar{c}_{\text{model},n}}{\bar{c}_{\text{exp},n}}\right| \times 100\% \tag{41}$$

$$\text{MAPE}_{\text{sim}} = \frac{1}{N}\sum_{n=1}^{N}\left|\frac{\bar{c}_{\text{sim},n} - \bar{c}_{\text{model},n}}{\bar{c}_{\text{sim},n}}\right| \times 100\% \tag{42}$$

Here, N is the number of data points considered. MAPE_{exp} and MAPE_{sim} values for all models are shown in Figure 3. As the finite volume simulation solves the most comprehensive set of physical equations of all models considered, simulation values are used as a reference to account for the possible presence of error or scattering associated with the experimental data points. Note that due to the difference in measurement methods (discussed in Section 4.2),

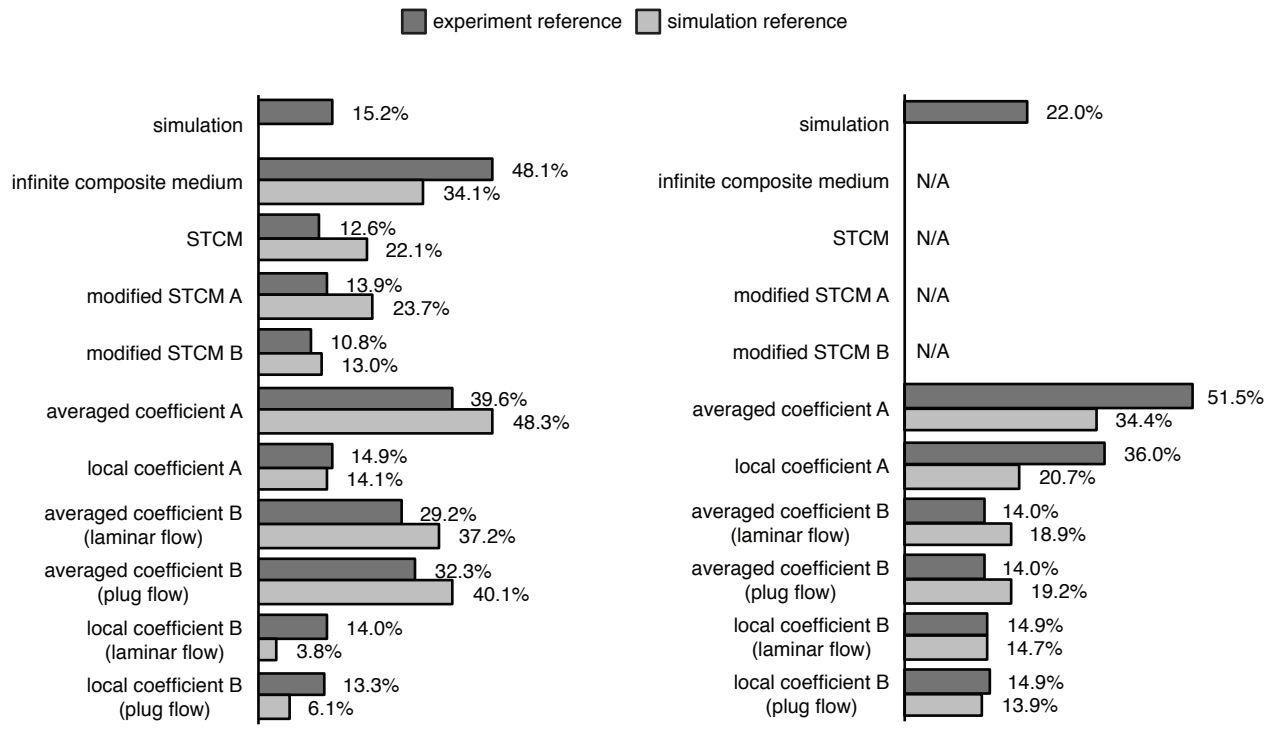

(a) 8HQ data

(b) methyl red data

Fig. 3: MAPE values for all models using (a) 8HQ experimental data of Ciceri et al. (2011a) and (b) methyl red data of Surmeian et al. (2002). $MAPE_{exp}$ and $MAPE_{sim}$ defined in Eqs. 41 and 42

velocity-averaged simulation concentrations were used in the $MAPE_{sim}$ denominator for the 8HQ data (Ciceri et al. 2011a) and area-averaged simulation concentrations were used for the methyl red data (Surmeian et al. 2002).

5.1 Finite volume simulation

As shown in Figure 3, the finite volume simulations were found to have values of $MAPE_{exp}$ of less than 22% for both data sets. Example cross-sectional distributions of the 8HQ concentration are shown in Figure 4. For all flow rates shown, the highest gradients in solute

concentration occur close to the inlet of the microchannel and are localised close to the interface. This explains why the deviation between the simulation line profile and simulation area-averaged concentrations decreases with increasing x/L, as shown in Figure 2. The presence of curving in the concentration contours as a result of the laminar flow profile, or 'butterfly effect' (Ismagilov et al. 2000; Kamholz et al. 1999), was observed in the simulations.

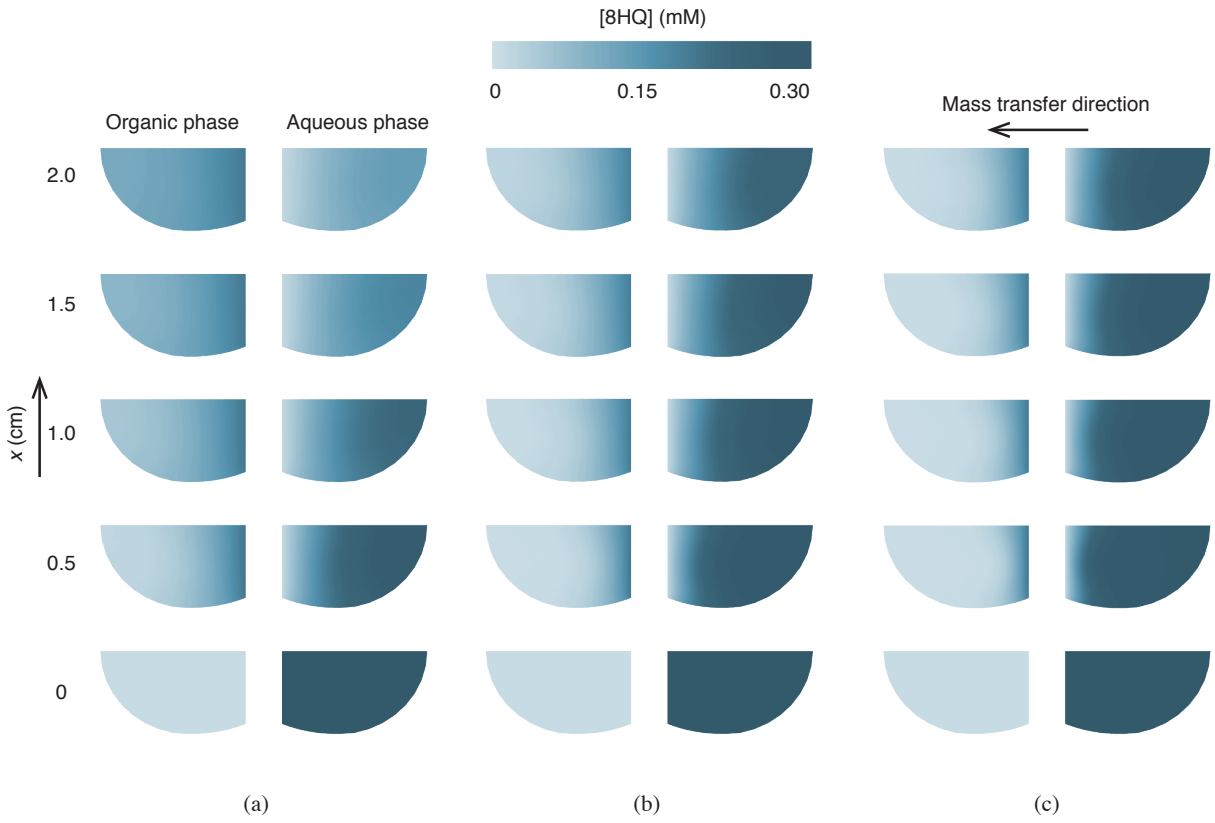

Fig. 4: Cross-sectional distribution of 8HQ concentration for (a) $\{F_{\text{org}}, F_{\text{aq}}\} = \{0.23, 0.15\}$ mL/hr, (b) $\{0.75, 0.39\}$ mL/hr, (c) $\{1.84, 0.86\}$ mL/hr

5.2 Infinite composite medium model

As shown in Figure 3a, the $\mathrm{MAPE}_{\mathrm{exp}}$ value for the infinite composite medium model was high (of order 50% for the experimental data of Ciceri et al. (2011a)). The model is not applicable to the methyl red data of Surmeian et al. (2002) due to failure of the constraint $t^* \ll h_{\mathrm{norm}}^2/\mathscr{D}_i$. The high error associated with the infinite composite medium model is consistent with the approximations implicit in the model. The model uses a one-dimensional approximation of the complex geometry and does not account for the effect of dispersion due to the non-uniform velocity profile. This model assumes the solute concentration is constant on both walls, as well as at the interface. From Figure 4, it can be seen that the solute concentration does not remain constant on the outer walls for the time scales associated with the experiment.

5.3 Mass transfer coefficient models

The mass transfer coefficient models, in particular those based on the local mass transfer coefficient, were associated with low values of the MAPE. Basing a model on the local mass transfer coefficient ('local coefficient A & B') resulted in more accurate results than using the average transfer coefficient ('averaged coefficient A & B'). As shown in Figure 3, a reduction in both $\mathrm{MAPE}_{\mathrm{exp}}$ and $\mathrm{MAPE}_{\mathrm{sim}}$ was achieved for all local coefficient models in comparison to the corresponding averaged coefficient model.

Figure 5 shows the x-dependency of the phase-specific local mass transfer coefficients. When calculated using penetration theory (Eq. 28), the local transfer coefficients approach zero as x, or equivalently t, approaches infinity. This is not consistent with the use of the correlations of van Male et al. (2004) (Eqs. 31 and 33), in which the local transfer coefficient has a non-zero horizontal asymptote. The plug flow correlation (Eq. 33) was found to diverge

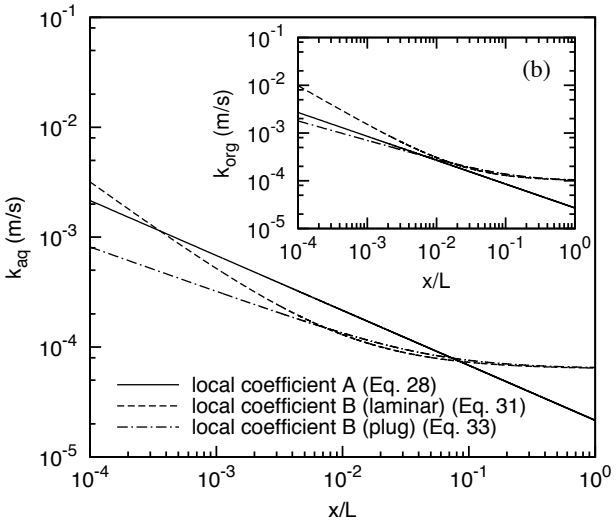

(a)

Fig. 5: Example local mass transfer coefficient x-dependency for: (a) aqueous phase, (b) organic phase (see inset). The contact time scale has been arbitrarily set to $t^* = 1$ s for both phases

from the laminar flow correlation (Eq. 31) at low values of x/L. The similarity of the local transfer coefficient values in the region $x/L > 10^{-2}$ explains the closeness in results when either averaged laminar or plug flow coefficients were used ('averaged coefficient B'). Values for $x/L < 10^{-2}$ do not contribute significantly to the integral average over the entire domain.

As shown in Figure 3, use of the correlation of van Male et al. (2004) ('local and averaged coefficient B') resulted in a lower value of both MAPE_{exp} and MAPE_{sim} than estimating the transfer coefficient using penetration theory ('local and averaged coefficient A'). Using Eq. 31 ('averaged coefficient B'), $\tilde{Sh}_i$ were found to range between 2.7–3.9 for the aqueous phase and 2.7–4.3 for the organic phase ($\tilde{Sh}_i$ values are tabulated in Online Resource 1). Note that Eq. 31 was originally determined from a regression to CFD simulation results, while Eq. 33 was derived using an analytical solution to a two-dimensional diffusion equation with a constant velocity profile. For this reason, Eq. 31 captures the effect of the velocity

profile on solute dispersion, whereas Eq. 33 will introduce an error due to the assumption of a uniform velocity profile (plug flow). When comparing the averaged coefficient results to the simulation, which *does* account for dispersion due to the velocity profile, the value of $\mathrm{MAPE}_{\mathrm{sim}}$ increased for all cases. For the local coefficient models, the value of $\mathrm{MAPE}_{\mathrm{sim}}$ remained approximately constant.

5.4 Static transfer cell models

Results using the STCM and modified STCM are shown in Table 5 for the experimental data of Ciceri et al. (2011a). The static transfer cell models cannot be applied to the methyl red data of Surmeian et al. (2002) as the time constraint $t^* \ll h_{\mathrm{norm}}^2/\mathscr{D}_i$ is not satisfied for the experimental conditions used. As shown in Figure 3a, use of the interfacial contact time t_{int} ('modified STCM B') resulted in lower values of both $\mathrm{MAPE}_{\mathrm{exp}}$ and $\mathrm{MAPE}_{\mathrm{sim}}$ than using the organic phase residence time t_{org} (STCM).

A comparison between the experimental organic phase residence time t_{org} and the simulated interfacial contact time t_{int} for the 8HQ data is shown in Figure 6. For all flow rates used, the interfacial contact time was found to be greater than the organic phase residence time. Similar results have been obtained for a homogeneous system (Hotta et al. 2007).

Interfacial velocities were also obtained using the thin slit result of Eq. 39. As shown in Figure 6, the interfacial contact time did not match that of simulation, but rather approximately equaled t_{org} for all values of t_{org}. The two-dimensional nature of the thin slit model implicitly assumes that the depth of the microchannel does not affect the shape of the velocity profile. As noted by Pohar et al. (2012), the formation of laminar planar interfaces in heterogeneous systems requires a high width-to-depth aspect ratio. For the present systems, the ratio of the maximum channel x-width to maximum channel z-depth was approximately

Table 5: Outlet 8HQ concentrations (mM) of all models for the corresponding experimental data of Ciceri et al. (2011a): (a) aqueous phase, (b) organic phase

	Quantity	Flow rate (mL/hr) and concentration (mM)				
(a)	F_{aq} (mL/hr)	0.86	0.60	0.39	0.23	0.15
	experiment	0.17 ± 0.01	0.16 ± 0.003	0.15 ± 0.003	0.094 ± 0.006	0.094 ± 0.02
	simulation	0.180	0.165	0.140	0.105	0.074
	infinite composite medium	0.195	0.176	0.158	0.130	0.104
	STCM	0.206	0.189	0.172	0.138	0.095
	modified STCM A	0.203	0.189	0.171	0.140	0.105
	modified STCM B	0.196	0.178	0.159	0.125	0.086
	averaged coefficient A	0.219	0.207	0.196	0.177	0.155
	local coefficient A	0.174	0.166	0.148	0.128	0.117
	averaged coefficient B	0.226	0.210	0.193	0.155	0.108
	local coefficient B	0.187	0.170	0.143	0.103	0.070
(b)	F_{org} (mL/hr)	1.84	1.12	0.75	0.41	0.23
	experiment	0.035 ± 0.005	0.043 ± 0.003	0.051 ± 0.0001	0.073 ± 0.003	0.112 ± 0.001
	simulation	0.040	0.054	0.065	0.090	0.125
	infinite composite medium	0.071	0.088	0.103	0.125	0.143
	STCM	0.028	0.041	0.049	0.072	0.111
	modified STCM A	0.029	0.041	0.050	0.071	0.105
	modified STCM B	0.033	0.047	0.055	0.079	0.118
	averaged coefficient A	0.022	0.031	0.036	0.050	0.073
	local coefficient A	0.042	0.053	0.061	0.077	0.097
	averaged coefficient B	0.019	0.030	0.038	0.062	0.103
	local coefficient B	0.036	0.051	0.063	0.091	0.128

3.6 for the 8HQ experiments and 9.1 for the methyl red experiments. This means that the two-dimensional thin slit approximation for this system is invalid. Hence, in the absence of t_{int} values determined using numerical simulation, it is suggested that the organic phase residence time t_{org} be used as the contact time scale as opposed to the value determined using the thin slit result.

5.5 Model comparison

The different models examined are each associated with assumptions that approximate the physical reality of the diffusion experiment. The infinite composite medium model (Eqs. 17 and 18) is based on constant wall concentration boundary conditions. Finite volume simulation results in Figure 4 show that these boundary conditions are not generally applicable

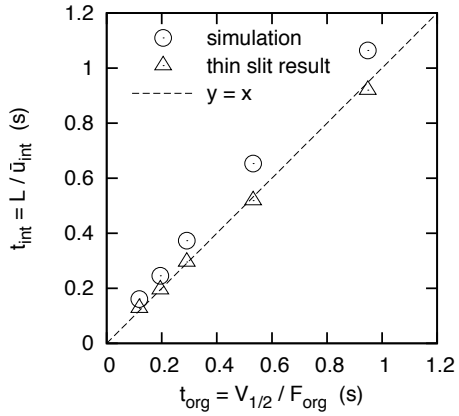

Fig. 6: Example parity plot of interfacial contact time t_{int}, determined by: (i) averaging the interfacial velocity from two-dimensional finite volume simulations or (ii) use of a thin slit result (Bird et al. 2002), against organic phase residence time t_{org}. Experimental geometry and flow rates from Ciceri et al. (2011a) are used

for $x \gtrsim 1$ cm, as each wall concentration deviates from its initial value when the phase flow rates are low. The infinite composite medium model is also based on a one-dimensional approximation of a complex geometry and does not account for dispersion due to the velocity profile. The infinite composite medium model, where applicable, was associated with the highest value of $\mathrm{MAPE}_{\mathrm{exp}}$ out of all models considered.

The STCM models are based on the same one-dimensional diffusion equation as the infinite composite medium model (Eq. 16), however the no-flux boundary condition (Neumann condition) on the microchannel wall is more realistic than that of constant concentration (Dirichlet condition). This is consistent with the lower values of both $\mathrm{MAPE}_{\mathrm{exp}}$ and $\mathrm{MAPE}_{\mathrm{sim}}$ for the STCM model, where applicable, than the infinite composite medium model. The STCM model was found to improve when basing the pass length contact time on the interfacial velocity as opposed to the average velocity. For the 8HQ data, using t_{int} gave a $\mathrm{MAPE}_{\mathrm{sim}}$ value of 13.0% compared to 22.1% when using t_{org}.

The transfer coefficient models were found to have varying degrees of resultant error. Generally, use of average mass transfer coefficients ('averaged coefficient A & B') resulted in higher MAPE values than the use of local transfer coefficients ('local coefficient A & B'). The most accurate transfer coefficient model was 'local coefficient B' with $MAPE_{exp}$ and $MAPE_{sim}$ values of less than 15% for both data sets. This low error is consistent with the model accounting for dispersion by the velocity profile, which was not accounted for by any of the other analytical models. Use of the laminar flow correlation of van Male et al. (2004) (Eq. 31) was demonstrated to give lower values of $MAPE_{sim}$ for the 8HQ data than the plug flow correlation (Eq. 33), and lower or approximately similar values for the methyl red data.

The finite volume simulation solves the most comprehensive set of equations out of all models considered. The simulations account for the complex cross-sectional geometry of the system and account for effects of the velocity profile on dispersion of the solute. The two main assumptions associated with the simulations were covered in Sections 2.1 and 2.2: neglecting of the interfacial curvature and velocity development length. Note that these two assumptions were also employed in all of the analytical models considered. Hence, it is expected that the accuracy of any of the analytical models can approach, at best, that of the simulations. Thus, $MAPE_{sim}$ values can be interpreted as the ability of the analytical model to reproduce the underlying diffusion equations, given the assumptions common to all predictive methods used. The simulation also allows determination of both area-averaged and velocity-averaged concentrations. Simulation velocity-averaged results (not shown) and area-averaged results, however, were found to have a maximum difference of 1% for the aqueous phase. Therefore, in this system, the velocity-averaged output from the transfer coefficient model was judged to be representative of an area-averaged concentration.

Of the analytical models used, the 'local coefficient B' model was found to have the ideal combination of low values of $MAPE_{exp}$ and $MAPE_{sim}$, together with a greater range

of applicability (the infinite composite medium and STCM models are subject to the short time scale restrictions $t^* \ll D_h^2/\mathscr{D}_i$ and $t^* \ll h_{norm}^2/\mathscr{D}_i$). If detailed CFD type models are not practical, it is recommended that the 'local coefficient B' model be used for the Y-Y design, using a local mass transfer coefficient based on the laminar flow correlation of van Male et al. (2004) (Eq. 31).

6 Conclusions

A finite volume simulation has been used to model existing experimental data for interfacial solute diffusion in a microchannel. The steady-state Navier-Stokes equations were first solved on a two-dimensional plane before the solution was extruded through a three-dimensional volume, allowing the advection-diffusion equation governing the concentration profile to be solved efficiently. The simulation methodology is novel in that it makes use of split flow domains to accurately treat jump discontinuities in both concentrations and physical properties across the interface. The simulation also accounted for the complex cross-sectional geometry of the microchannel.

Analytical approaches including an infinite composite medium model, mass transfer coefficient models and a static transfer cell model were assessed. The infinite composite medium model resulted in the highest error when compared to the experimental results of Ciceri et al. (2011a). The static transfer cell models showed good agreement with the same data, however are subject to restrictions on the experimental time scale. An increase in accuracy can be achieved for the static transfer cell model by basing the characteristic time scale on the interfacial contact time (determined using CFD), as opposed to the organic phase residence time. Mass transfer coefficient models were found to give accurate results when based on the local mass transfer coefficient. The most accurate method of estimating

the local mass transfer coefficient was found to be the laminar flow correlation of van Male et al. (2004).

Use of CFD techniques is recommended for reliable and accurate results, with a maximum mean absolute percentage error (MAPE) of 22% for all experimental data considered. Mass transfer coefficient models, however, have been shown to give low MAPE values and are recommended for use as a first approximation of the system. Application of the simulation technique and analytical models is envisaged in the determination of reaction rate constants for μSX experiments as detailed in Part II of this study (Ciceri et al. 2012).

Acknowledgements Support from the Australian Research Council and the Particulate Fluids Processing Centre is gratefully acknowledged.

References

Akpa BS, Matthews SM, Sederman AJ, Yunus K, Fisher AC, Johns ML, Gladden LF (2007) Study of miscible and immiscible flows in a microchannel using Magnetic Resonance Imaging. Anal Chem 79(6128-6134)

Aota A, Hibara A, Kitamori T (2007) Pressure balance at the liquid-liquid interface of micro countercurrent flows in microchips. Anal Chem 79(10):3919–3924

Aota A, Mawatari K, Kitamori R (2009) Parallel multiphase microflows: fundamental physics, stabilization methods and applications. Lab Chip 9:2470–2476

Bird RB, Stewart WE, Lightfoot EN (2002) Transport Phenomena, 2nd edn. John Wiley & Sons, Inc.

Broboana D, Balan CM, Wohland T, Balan C (2011) Investigations of the unsteady diffusion process in microchannels. Chem Eng Sci 66(9):1962–1972

Ciceri D, Perera JM, Stevens GW (2011a) A study of molecular diffusion across a water/oil interface in a Y-Y shaped microfluidic device. Microfluid Nanofluid 11(5):593–600

Ciceri D, Perera JM, Stevens GW (2011b) Extraction of Co(II) by di (2-ethylhexyl) phosphoric acid in a microfluidic device. In: Int Solvent Extr Conf (ISEC 2011), Santiago, Chile, ISEC, Santiago, Chile, p 112

Ciceri D, Mason LR, Harvie DJE, Perera JM, Stevens GW (2012) Modelling of interfacial mass transfer in microfluidic solvent extraction. Part II. Heterogeneous transport with reaction. Microfluid Nanofluid

Submitted

Crank J (1975) Diffusion in a plane sheet. In: The Mathematics of Diffusion, 2nd edn, Clarendon Press, Oxford, chap 3

Fick AE (1855) On liquid diffusion. Philos Mag 4(10):30–39

Frank-Kamenetskii DA (1969) Diffusion and Heat Transfer in Chemical Kinetics, 2nd edn. Plenum Press, New York

George PL, Borouchaki H (1998) Delaunay Triangulation and Meshing: Application to Finite Elements. Hermes

Geuzaine C, Remacle JF (2009) Gmsh: A 3-D finite element mesh generator with built-in pre- and post-processing facilities. Int J Numer Meth Eng 79(11):1309–1331

Harada M, Iwamoto K, Kitamori T, Sawada T (1993) Photothermal microscopy with excitation and probe beams coaxial under the microscope and its application to microparticle analysis. Anal Chem 65(20):2938–2940

Harvie DJE (2012) An implicit finite volume method for arbitrary transport equations. ANZIAM J 52:C1126–C1145

Higbie R (1935) The rate of absorption of a pure gas into a still liquid during a short time of exposure. Trans AIChE 31:365

Hotokezaka H, Tokeshi M, Harada M, Kitamori T, Ikeda Y (2005) Development of the innovative nuclide separation system for high-level radioactive waste using microchannel chip-extraction behavior of metal ions from aqueous phase to organic phase in microchannel. Prog Nucl Energ 47(1–4):439–447

Hotta T, Nii S, Yajima T, Kawaizumi F (2007) Mass tansfer characteristics of a microchannel device of split-flow type. Chem Eng Technol 30(2):208–213

Ismagilov RF, Stroock AD, Kenis PJA, Whitesides G, Stone HA (2000) Experimental and theoretical scaling laws for transverse diffusive broadening in two-phase laminar flows in microchannels. Applied Physics Letters 76(17):2376–2378

Kamholz AE, Yager P (2001) Theoretical analysis of molecular diffusion in pressure-driven laminar flow in microfluidic channels. Biophys J 80(1):155–160

Kamholz AE, Weigl BH, Finlayson BA, Yager P (1999) Quantitative analysis of molecular interaction in a microfluidic channel: The T-sensor. Anal Chem 71:5340–5347

Kuban J, Dasgupta P, Berg PK (2003) Vertically stratified flows in microchannels. Computational simulations and applications to solvent extraction and ion exchange. Anal Chem 75(14):3549–3556

van Leeuwen M, Li X, Krommenhoek EE, Gardeniers H, Ottens M, van der Wielen LAM, Heijnen JJ, van Gulik WM (2009) Quantitative determination of glucose transfer between cocurrent laminar water streams in a H-shaped microchannel. Biotechnol Progr 25(6):1826–1832

Lide DR (2009) CRC Handbook of Chemistry and Physics, 90th edn. Boca Raton, CRC Press

van Male P, de Croon MHJM, Tiggelaar RM, van den Berg A, Schouten JC (2004) Heat and mass transfer in a square microchannel with asymmetric heating. Int J Heat Mass Tran 47(1):87 – 99

McCulloch JK, Kelly ED, Perera JM, White LR, Stevens GW, Grieser F (1996) Direct spectroscopic measurement and theoretical modeling of the diffusion of a single species in a two-phase unstirred system. J Colloid and Interf Sci 184(2):399–405

Minagawa T, Tokeshi M, Kitamori T (2001) Integration of a wet analysis system on a glass chip: Determination of Co (II) as 2-nitroso-1-naphthol chelates by solvent extraction and Thermal Lens Microscopy. Lab Chip 1(1):72–75

Nadim A, Borhan A, Haj-Hariri H (1996) Tangential stress and Marangoni effects at a fluid-fluid interface in a Hele-Shaw cell. J Colloid Interf Sci 181:159–164

Nishi K, Perera JM, Misumi R, Kaminoyama M, Stevens GW (2010) Study of diffusion of Co(II) and Co(II)-DEHPA complex in a microfluidic device. J Chem Eng Jpn 43(4):342–348

Nishi K, Perera JM, Misumi R, Kaminoyama M, Stevens GW (2011) Flow and diffusion behaviour as a function of viscosity in a double-Y-type microfluidic device. J Chem Eng Jpn 44(7):509–517

Perry RH, Green DW (2007) Perry's Chemical Engineers' Handbook, 8th edn. McGraw-Hill, New York

Pohar A, Lakner M, Plazl I (2012) Parallel flow of immiscible liquids in a microreactor: modeling and experimental study. Microfluid Nanofluid 12:307–316

Sato K, Tokeshi M, Sawada T, Kitamori T (2000) Molecular transport between two phases in a microchannel. Anal Sci 16:455–456

Smirnova A, Mawatari K, Hibara A, Proskurnin MA, Kitamori T (2006) Micro-multiphase laminar flows for the extraction and detection of carbaryl derivative. Anal Chim Acta 558(1-2):69–74

Squires TM, Quake SR (2005) Microfluidics: Fluid physics at the nanoliter scale. Rev Mod Phys 77(3):977–1026

Surmeian M, Slyadnev MN, Hisamoto H, Hibara A, Uchiyama K, Kitamori T (2002) Three-layer flow membrane system on a microchip for investigation of molecular transport. Anal Chem 74(9):2014–2020

Tetala KKR, Swarts JW, Chen B, Janssen AEM, van Beek TA (2009) A three-phase microfluidic chip for rapid sample clean-up of alkaloids from plant extracts. Lab Chip 9(14):2085–2092

Tokeshi M, Minagawa T, Kitamori T (2000) Integration of a microextraction system on a glass chip: Ion-pair solvent extraction of Fe(II) with 4,7-diphenyl-1,10-phenanthrolinedisulfonic acid and tri-*n*-octylmethylammonium chloride. Anal Chem 72(7):1711–1714

Truskey GA, Yuan F, Katz DF (2004) Transport Phenomena in Biological Systems (Chapter 7), 1st edn. Prentice Hall

Žnidaršič-Plazl P, Plazl I (2007) Steroid extraction in a microchannel system – mathematical modelling and experiments. Lab Chip 7:883–889

Whitesides G (2006) The origins and the future of microfluidics. Nature 442:368–373

Yaws CL (2003) Yaws' Handbook of Thermodynamic and Physical Properties of Chemical Compounds. Knovel

A Mass transfer coefficient model

A.1 Derivation

The local flux J_y of solute in the y-direction is defined by

$$J_y = k_{\mathrm{aq}}(\bar{c}_{\mathrm{aq}} - c_{\mathrm{aq,int}}) \tag{A.1}$$

$$= k_{\mathrm{org}}(c_{\mathrm{org,int}} - \bar{c}_{\mathrm{org}})\,, \tag{A.2}$$

where k_{aq} and k_{org} are the local mass transfer coefficients, $c_{i,\mathrm{int}}$ are the interfacial concentrations (per volume basis) and $\bar{c}_i$ are the velocity-averaged solute concentrations given by

$$\bar{c}_i = \frac{\int_{A_{\perp,i}} c_i u_i \,\mathrm{d}A}{\int_{A_{\perp,i}} u_i \,\mathrm{d}A}\,, \tag{A.3}$$

where $A_{\perp,i}$ is the cross-sectional area of the relevant half of the channel. The distribution coefficient is defined, using Eq. 11, by

$$c_{\mathrm{org,int}} = K_{\mathrm{D}} c_{\mathrm{aq,int}} \,. \tag{A.4}$$

Substituting Eq. A.4 into Eq. A.2 gives

$$J_y = k_{\mathrm{org}} (K_{\mathrm{D}} c_{\mathrm{aq,int}} - \bar{c}_{\mathrm{org}}) \,. \tag{A.5}$$

Eliminating $c_{\mathrm{aq,int}}$ gives

$$J_y \left(\frac{1}{k_{\mathrm{aq}}} + \frac{1}{k_{\mathrm{org}} K_{\mathrm{D}}} \right) = \bar{c}_{\mathrm{aq}} - \frac{\bar{c}_{\mathrm{org}}}{K_{\mathrm{D}}} \,. \tag{A.6}$$

For convenience, the following definitions are introduced:

$$\Delta \bar{c} \stackrel{\mathrm{def}}{=} \bar{c}_{\mathrm{aq}} - \frac{\bar{c}_{\mathrm{org}}}{K_{\mathrm{D}}} \tag{A.7}$$

$$K_{\mathrm{eff}} \stackrel{\mathrm{def}}{=} \left(\frac{1}{k_{\mathrm{aq}}} + \frac{1}{k_{\mathrm{org}} K_{\mathrm{D}}} \right)^{-1} \tag{A.8}$$

so that

$$J_y = K_{\mathrm{eff}} \Delta \bar{c} \,. \tag{A.9}$$

From the definition of J_y (Eq. A.2),

$$J_y \, \mathrm{d}A = F_{\mathrm{aq}} \left[\bar{c}_{\mathrm{aq}}(A) - \bar{c}_{\mathrm{aq}}(A + \mathrm{d}A) \right] \tag{A.10}$$

$$= F_{\mathrm{org}} \left[\bar{c}_{\mathrm{org}}(A + \mathrm{d}A) - \bar{c}_{\mathrm{aq}}(A) \right] \,. \tag{A.11}$$

Combining Eqs. A.10 and A.11 gives

$$\begin{aligned} J_y \, \mathrm{d}A \left(\frac{1}{F_{\mathrm{aq}}} + \frac{1}{F_{\mathrm{org}}} K_{\mathrm{D}} \right) = \\ - \left[\bar{c}_{\mathrm{aq}}(A + \mathrm{d}A) - \bar{c}_{\mathrm{aq}}(A) - \left(\frac{\bar{c}_{\mathrm{org}}(A + \mathrm{d}A)}{K_{\mathrm{D}}} - \frac{\bar{c}_{\mathrm{org}}(A)}{K_{\mathrm{D}}} \right) \right] \,. \end{aligned} \tag{A.12}$$

Using the definition from Eq. A.7 and taking the limit $\mathrm{d}A \to 0$ gives

$$J_y \left(\frac{1}{F_{\mathrm{aq}}} + \frac{1}{F_{\mathrm{org}} K_{\mathrm{D}}} \right) = - \frac{\mathrm{d}\Delta \bar{c}}{\mathrm{d}A} \,. \tag{A.13}$$

Substituting Eq. A.9 gives

$$\frac{\mathrm{d}\Delta\bar{c}}{\mathrm{d}A} = -K_{\mathrm{eff}}\left(\frac{1}{F_{\mathrm{aq}}} + \frac{1}{F_{\mathrm{org}}K_{\mathrm{D}}}\right)\Delta\bar{c}\,. \tag{A.14}$$

Integrating this expression gives

$$\ln\left(\frac{\Delta\bar{c}_{\mathrm{outlet}}}{\Delta\bar{c}_{\mathrm{inlet}}}\right) = -K_{\mathrm{eff}}\left(\frac{1}{F_{\mathrm{aq}}} + \frac{1}{F_{\mathrm{org}}K_{\mathrm{D}}}\right)A_{\mathrm{ref}}\,, \tag{A.15}$$

where A_{ref} is the total area of the interface. The total amount of solute transferred across the interface is given by

$$\tilde{J}_{\mathrm{y}}A_{\mathrm{ref}} = F_{\mathrm{aq}}(\bar{c}_{\mathrm{aq,inlet}} - \bar{c}_{\mathrm{aq,outlet}}) \tag{A.16}$$

$$= F_{\mathrm{org}}(\bar{c}_{\mathrm{org,outlet}} - \bar{c}_{\mathrm{org,inlet}})\,, \tag{A.17}$$

where $\tilde{J}_{\mathrm{y}}$ is the average flux of solute. Combining Eqs. A.16 and A.17 gives

$$\begin{aligned}\tilde{J}_{\mathrm{y}}A_{\mathrm{ref}}\left(\frac{1}{F_{\mathrm{aq}}} + \frac{1}{F_{\mathrm{org}}K_{\mathrm{D}}}\right) &= \bar{c}_{\mathrm{aq,inlet}} - \bar{c}_{\mathrm{aq,outlet}} + \frac{\bar{c}_{\mathrm{org,outlet}}}{K_{\mathrm{D}}} - \frac{\bar{c}_{\mathrm{org,inlet}}}{K_{\mathrm{D}}} \\ &= \Delta\bar{c}_{\mathrm{inlet}} - \Delta\bar{c}_{\mathrm{outlet}}\,. \end{aligned} \tag{A.18}$$

Combing Eqs. A.15 and (A.18) gives

$$\tilde{J}_{\mathrm{y}} = K_{\mathrm{eff}}\frac{\Delta\bar{c}_{\mathrm{outlet}} - \Delta\bar{c}_{\mathrm{inlet}}}{\ln\left(\dfrac{\Delta\bar{c}_{\mathrm{outlet}}}{\Delta\bar{c}_{\mathrm{inlet}}}\right)} \tag{A.19}$$

$$= K_{\mathrm{eff}}\,(\Delta\bar{c})_{\mathrm{LM}}\,. \tag{A.20}$$

A.2 Solution method

The aim is to solve for $\bar{c}_{\mathrm{org,outlet}}$ for a fixed experimental $\Delta\bar{c}_{\mathrm{inlet}}$. From mass conservation,

$$F_{\mathrm{aq}}\bar{c}_{\mathrm{aq,outlet}} + F_{\mathrm{org}}\bar{c}_{\mathrm{org,outlet}} = F_{\mathrm{aq}}\bar{c}_{\mathrm{aq,inlet}} + F_{\mathrm{org}}\bar{c}_{\mathrm{org,inlet}}\,. \tag{A.21}$$

Substituting

$$\bar{c}_{\mathrm{org,outlet}} = K_{\mathrm{D}}(\bar{c}_{\mathrm{aq,outlet}} - \Delta\bar{c}_{\mathrm{outlet}}) \tag{A.22}$$

into Eq. A.21 gives

$$\bar{c}_{\mathrm{aq,outlet}} = \frac{1}{F_{\mathrm{aq}} + K_{\mathrm{D}}F_{\mathrm{org}}}\left(F_{\mathrm{aq}}\bar{c}_{\mathrm{aq,inlet}} + F_{\mathrm{org}}\bar{c}_{\mathrm{org,inlet}} + F_{\mathrm{org}}\Delta\bar{c}_{\mathrm{outlet}}\right), \tag{A.23}$$

where, for constant values of $\tilde{k}_i$ ('averaged coefficient A & B'), $\Delta\bar{c}_{\mathrm{outlet}}$ is determined from Eq. A.15,

$$\Delta\bar{c}_{\mathrm{outlet}} = \Delta\bar{c}_{\mathrm{inlet}}\exp\left[-K_{\mathrm{eff}}\left(\frac{1}{K_{\mathrm{D}}F_{\mathrm{aq}}} + \frac{1}{F_{\mathrm{org}}}\right)A_{\mathrm{ref}}\right]. \tag{A.24}$$

Eq. A.24 is substituted into Eq. A.23 in order to determine $\bar{c}_{\mathrm{aq,outlet}}$. $\bar{c}_{\mathrm{org,outlet}}$ can then be determined from Eq. A.22.

For x-dependent k_i values ('local coefficient A & B'), $\Delta\bar{c}_{\mathrm{outlet}}$ is determined using numerical integration:

$$\Delta\bar{c}_{\mathrm{outlet}} = \Delta\bar{c}_{\mathrm{inlet}}\exp\left[-\left(\frac{1}{F_{\mathrm{aq}}} + \frac{1}{F_{\mathrm{org}}K_{\mathrm{D}}}\right)\int_0^L K_{\mathrm{eff}}(x)d\,\mathrm{d}x\right], \tag{A.25}$$

where

$$K_{\mathrm{eff}}(x) = \left(\frac{1}{k_{\mathrm{aq}}(x)} + \frac{1}{k_{\mathrm{org}}(x)K_{\mathrm{D}}}\right)^{-1} \tag{A.26}$$

and

$$k_i(x) = \frac{\mathscr{D}_i}{D_{\mathrm{h}}}Sh_i(x). \tag{A.27}$$

Here, the substitution $\mathrm{d}A = d\,\mathrm{d}x$ has been made, where d is the z-height of the interface. The same solution method for determining $\bar{c}_{\mathrm{org,outlet}}$ then follows as per the constant k_i case.

B Analytical expression for a heterogeneous thin slit

Building on the approach of Bird et al. (2002), an analytical expression was derived for two immiscible, incompressible liquids flowing in the y-direction of a thin slit of length L and effective width $2D_{\mathrm{h}}$. The momentum flux for each phase i is given by the differential equation

$$\frac{\mathrm{d}\tau_{yx,i}}{\mathrm{d}y} = \frac{\Delta p_i}{L}, \tag{B.1}$$

where Δp_i is the phase-specific pressure difference between the pass length inlet and outlet. Integrating Eq. B.1 for each phase gives

$$\tau_{yx,i} = \left(\frac{\Delta p_i}{L}\right) y + \alpha_i \,, \tag{B.2}$$

where α_i is a constant of integration. The momentum flux across the interface (located at $y = 0$) is assumed to be balanced:

$$\begin{aligned} \tau_{yx,1}\big|_{y\to 0^-} &= \tau_{yx,2}\big|_{y\to 0^+} \\ \Rightarrow \alpha_1 &= \alpha_2 \stackrel{\text{def}}{=} \alpha \,. \end{aligned} \tag{B.3}$$

Substituting Newtons's law of viscosity and integrating gives

$$u_{x,i} = -\frac{1}{2\mu_i}\frac{\Delta p_i}{L} y^2 - \frac{\alpha}{\mu_i} y + \beta_i \,. \tag{B.4}$$

The solvent velocity was assumed to be continuous across the interface:

$$\begin{aligned} u_{x,1}\big|_{y\to 0^-} &= u_{x,2}\big|_{y\to 0^+} \\ \Rightarrow \beta_1 &= \beta_2 \stackrel{\text{def}}{=} \beta \,. \end{aligned} \tag{B.5}$$

This gives a set of two equations to be solved simultaneously:

$$u_{x,i} = -\frac{1}{2\mu_i}\frac{\Delta p_i}{L} y^2 - \frac{\alpha}{\mu_i} y + \beta \,. \tag{B.6}$$

A no-slip boundary condition was applied on two fictional walls, each a distance D_h from the centreline:

$$u_{x,1}\big|_{y=-D_\mathrm{h}} = 0 \,; \quad u_{x,2}\big|_{y=D_\mathrm{h}} = 0 \,. \tag{B.7}$$

Solving for α and β gives:

$$\alpha(\Delta p_1, \Delta p_2) = \frac{D_\mathrm{h}}{2L}\left(\frac{\mu_2 \Delta p_1 - \mu_1 \Delta p_2}{\mu_1 + \mu_2}\right) \tag{B.8}$$

$$\beta(\Delta p_1, \Delta p_2) = \frac{D_\mathrm{h}^2}{2L}\left(\frac{\Delta p_1 + \Delta p_2}{\mu_1 + \mu_2}\right) \tag{B.9}$$

The average velocities $\bar{u}_{x,i}$ are then given by:

$$\begin{aligned}\bar{u}_{x,1} &= \frac{1}{D_\mathrm{h}}\int_{-D_\mathrm{h}}^{0} u_{x,1}(y)\,\mathrm{d}y \\ &= -\frac{1}{2\mu_1}\frac{\Delta p_1}{L}\frac{D_\mathrm{h}^2}{3} + \alpha(\Delta p_1,\Delta p_2)\frac{D_\mathrm{h}}{2\mu_1} + \beta(\Delta p_1,\Delta p_2) \qquad \text{(B.10)} \\ \bar{u}_{x,2} &= \frac{1}{D_\mathrm{h}}\int_{0}^{D_\mathrm{h}} u_{x,2}(y)\,\mathrm{d}y \\ &= -\frac{1}{2\mu_2}\frac{\Delta p_2}{L}\frac{D_\mathrm{h}^2}{3} - \alpha(\Delta p_1,\Delta p_2)\frac{D_\mathrm{h}}{2\mu_2} + \beta(\Delta p_1,\Delta p_2) \qquad \text{(B.11)}\end{aligned}$$

Eqs. B.10 and B.11 are solved simultaneously for Δp_i. The interfacial velocity is then given by

$$u_\mathrm{int} = \beta(\Delta p_1,\Delta p_2)\,. \qquad \text{(B.12)}$$

List of symbols

$A_{\perp,i}$	cross-sectional area of microchannel half-volume, (m^2)
A_ref	total area of interface, (m^2)
Bo	Bond number ($Bo = \Delta\rho g D_\mathrm{h}^2/\gamma$), (–)
c	local species concentration, (mM)
$\tilde{c}$	spatially-averaged species concentration, (mM)
$\bar{c}$	velocity-averaged species concentration, (mM)
d	z-height of interface, (m)
D_h	hydraulic diameter of microchannel half-volume, (m)
$\mathscr{D}$	diffusivity, (m^2/s)
F	volumetric flow rate, (m^3/s)
g	gravitational acceleration, (m/s^2)
Gz	mass transfer Graetz number ($Gz = Re\,Sc\,D_\mathrm{h}/x$), (–)
h_eq	equivalent height, (m)
h_norm	flow-rate-scaled equivalent height, (m)
$\boldsymbol{I}$	identity tensor, (–)
k_i	local mass transfer coefficient, (m/s)
$\tilde{k}_i$	average mass transfer coefficient, (m/s)

K_D	distribution coefficient, (–)
K_eff	effective mass transfer coefficient, (m/s)
L	microchannel pass length, (m)
$\hat{\mathbf{n}}$	unit normal vector, (–)
$\mathrm{MAPE}_\mathrm{exp}$	mean absolute percentage error (experimental reference), (–)
$\mathrm{MAPE}_\mathrm{sim}$	mean absolute percentage error (simulation reference), (–)
J_y	local diffusive flux of solute, (mol/m^2 s)
$\tilde{J}_y$	average diffusive flux of solute, (mol/m^2 s)
p	fluid pressure, (Pa)
R	interface radius of curvature, (m)
Re	Reynolds number ($Re = \rho \bar{u} D_\mathrm{h}/\mu$), (–)
Sc	Schmidt number ($Sc = \mu/\rho\mathscr{D}$), (–)
Sh	Sherwood number ($Sh = kD_\mathrm{h}/\mathscr{D}$), (–)
t	elapsed time of contact between phases, (s)
t^*	characteristic contact time scale (set either to t_org or t_int), (s)
t_int	interfacial contact time ($t_\mathrm{int} = L/\bar{u}_\mathrm{int}$), (s)
t_org	organic phase residence time ($t_\mathrm{org} = V_{1/2}/F_\mathrm{org}$), (s)
$\mathbf{u}$	fluid velocity, (m/s)
$\bar{u}_i$	mean fluid velocity, (m/s)
$\bar{u}_\mathrm{int}$	mean interfacial velocity, (m/s)
W	microchannel y-half-width, (m)
$V_{1/2}$	microchannel half-volume, (m^3)
x, y, z	Cartesian coordinates, (m)
$\tilde{y}$	maximum y-deformation of the interface, (–)

Greek letters

γ	interfacial tension, (N/m)
θ_max	maximum interfacial contact angle, (–)
ρ	fluid density, (kg/m^3)
$\boldsymbol{\tau}$	viscous stress tensor, (Pa)

μ	dynamic viscosity, (Pa s)
ϕ	maximum angle subtended by the interfacial arc, (rad)

Subscripts

0	initial
aq	aqueous phase
exp	experiment
i	ith phase
inlet	pass length inlet
int	interface
LM	logarithmic mean
max	maximum
n	nth data point
org	organic phase
outlet	pass length outlet
sim	simulation

Abbreviations

8HQ	8-hydroxyquinoline
CFD	Computational Fluid Dynamics
DEHPA	di-(2-ethylhexyl) phosphoric acid
LOC	Lab-on-a-Chip
MAPE	Mean Absolute Percentage Error
TLM	Thermal Lens Microscopy
TRM	tetramethyl rhodamine
STCM	Static Transfer Cell Model
SX	Solvent Extraction
μSX	Microfluidic Solvent Extraction